



Power Electronic Systems
Laboratory

© 2011 IEEE

IEEE Transactions on Industrial Electronics, Vol. 59, No. 1, pp. 194-210, January 2012.

Novel Hybrid Modulation Schemes Significantly Extending the Reactive Power Control Range of All Matrix Converter Topologies With Low Computational Effort

F. Schafmeister
J. W. Kolar

This material is posted here with permission of the IEEE. Such permission of the IEEE does not in any way imply IEEE endorsement of any of ETH Zurich's products or services. Internal or personal use of this material is permitted. However, permission to reprint/republish this material for advertising or promotional purposes or for creating new collective works for resale or redistribution must be obtained from the IEEE by writing to pubs-permissions@ieee.org. By choosing to view this document, you agree to all provisions of the copyright laws protecting it.



Eidgenössische Technische Hochschule Zürich
Swiss Federal Institute of Technology Zurich

Novel Hybrid Modulation Schemes Significantly Extending the Reactive Power Control Range of All Matrix Converter Topologies With Low Computational Effort

Frank Schafmeister, *Member, IEEE*, and Johann W. Kolar, *Fellow, IEEE*

Abstract—A novel approach based on indirect modulation, which significantly extends the reactive power control range for three-phase ac–ac matrix converters (MCs; applicable to all matrix topologies) and which is implementable with lowest computational effort, is proposed. This new method denoted as *hybrid modulation* facilitates the formation of reactive input current also for purely reactive load. The derivation of the modulation schemes, which rely on a decoupling of the output voltage and the reactive input current formation, is described in detail. Furthermore, the operating limits, i.e., the maximum reactive input current that could be formed for the given output voltage amplitude and load current amplitude, are determined. Finally, all theoretical considerations are verified by measurements taken on a 6.5-kW Very Sparse MC.

Index Terms—AC–AC power conversion, matrix converter (MC), modulation, reactive power control.

I. INTRODUCTION

SPARSE MATRIX converters (SMCs [1]; cf., Fig. 1) are functionally equivalent to Conventional MCs (CMCs) but are characterized by a lower realization effort and a lower control complexity. Consisting of two stages connected via a dc-link, SMCs are a topological variant of Indirect MCs (IMCs). By proper control of the input stage within each pulse half period, two line-to-line voltages are switched into the dc-link of the IMC. When the input stage is commutated at zero current (cf., i in Fig. 5) [1], [2], a multistep commutation scheme which has to be performed in dependence on the sign of the commutating voltage or current can be avoided. This results in low switching losses and high reliability, and it also enables operation of the Very Sparse MC [VSMC; Fig. 1(b)]. To commonly address CMC, IMC, SMC, and VSMC, the abbreviation MC is used.

In general, modulation schemes for MC can be classified into *direct* and *indirect* schemes [3], where the latter, being based on the assumption of a (virtual) dc-link, offer more simple

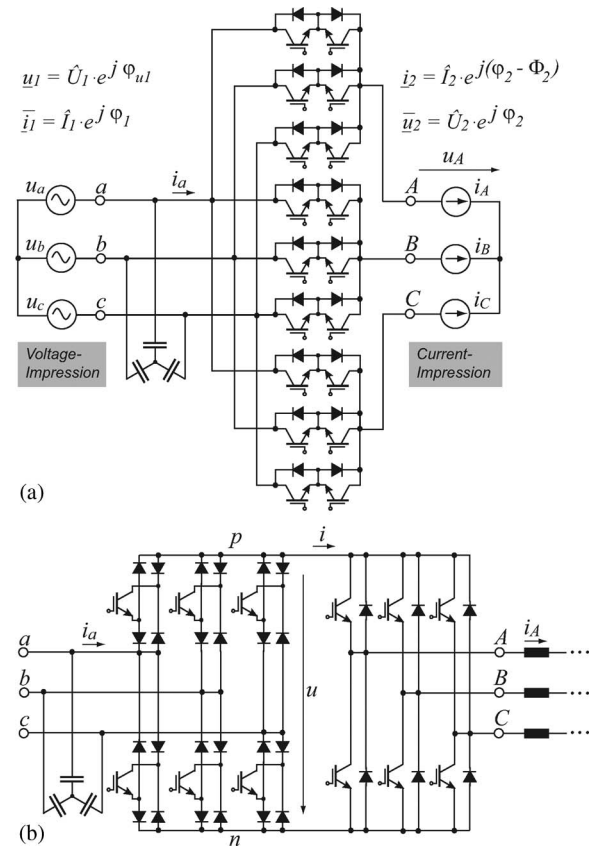


Fig. 1. Topology of (a) CMC and (b) VSMC according to [1].

modulation calculations and are the natural method for modulating IMC/SMCs containing physical dc-links. Traditionally, the maximization of the reactive input power that an MC could provide over the whole load range was not in the common focus of research. Indeed, conventional indirect modulation shows limited reactive input power generation capabilities in case of reactive load (cf., Fig. 2(a); $\Phi_2 > \pi/4$). Based on *direct* modulation, a method for maximizing the control range of a CMC was proposed in [4]. That method defines the control range reference but requires 24 equation systems to be solved online during each modulation period. Alternatively, an *indirect*-modulation-based *hybrid* scheme was introduced in [5]. This hybrid modulation principle that needs far less computational effort will be extended and further analyzed in

Manuscript received December 7, 2010; revised February 1, 2011; accepted February 8, 2011. Date of publication May 27, 2011; date of current version October 4, 2011. This work was supported by DELTA Energy Systems GmbH.

F. Schafmeister is with DELTA Energy Systems GmbH, 59494 Soest, Germany (e-mail: frank.schafmeister@delta-es.com).

J. W. Kolar is with the Power Electronic Systems Laboratory, Swiss Federal Institute of Technology (ETH) Zurich, 8092 Zurich, Switzerland (e-mail: kolar@lem.ee.ethz.ch).

Color versions of one or more of the figures in this paper are available online at <http://ieeexplore.ieee.org>.

Digital Object Identifier 10.1109/TIE.2011.2158045

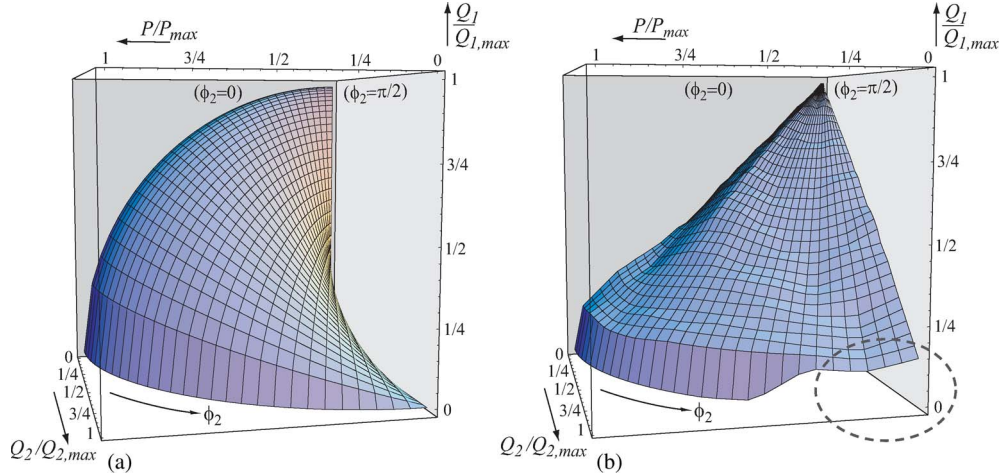


Fig. 2. Maximum control range of indirectly modulated MC. (a) Conventional indirect modulation. (b) Proposed hybrid modulation.

this paper, which also compiles the findings from [6] and [7], finally leading to an increased control range.

II. BASIC CONSIDERATIONS

The expressions in Fig. 1 describe the converters input and output voltages, as well as currents. Therefore, the input displacement angle is given implicitly with

$$\Phi_1 = \varphi_{u1} - \varphi_1. \quad (1)$$

Basically, Φ_1 and/or the input current vector position φ_1 can be freely adjusted to a desired reference by the modulation algorithm. The actual method of influencing Φ_1 is the core subject of this publication. On the one hand, the conventional indirect modulation [3] can be used. This used to be the only viable option so far—in the following, it will be referred to as *basic* modulation (index: *bas*). On the other hand, in [5], [6], and [8], the authors introduced a novel modulation approach which manipulates Φ_1 in a different and *independent* way compared to the basic modulation. Since the output voltage and the reactive input current formation are treated separately within this approach, the proposed scheme, which is still based on indirect modulation, will be denoted as *hybrid* modulation (index: *hyb*) in the following. Considering the previous statements, we can write $\Phi_1 = \Phi_{1,bas} + \Phi_{1,hyb}$, with $\Phi_{1,hyb} = 0$ for conventional basic modulation (abbreviation is $Q_{1,bas}$) and with $\Phi_{1,bas} = 0$ for hybrid modulation (abbreviation is $Q_{1,hyb}$).

A. Conventional Modulation as Basic Scheme ($\Phi_{1,hyb} = 0$)

For conventional modulation (being equivalent to indirect or virtual dc-link modulation of a CMC [3]), we have, for the relative turn-on times of the single switching states [5], e.g., for φ_1 in $-\pi/6, \dots, +\pi/6$ and φ_2 in $0, \dots, +\pi/3$ (as shown in Fig. 4)

$$d_{ab} = \cos(\varphi_1 + \pi/3) / \cos(\varphi_1)$$

$$d_{ac} = \cos(\varphi_1 - \pi/3) / \cos(\varphi_1)$$

$$\begin{aligned} \delta_{(100)} &= MU \cdot 1 / \cos(\Phi_{1,bas}) \cdot \cos(\varphi_1) \cdot \cos(\varphi_2 + \pi/6) \\ \delta_{(110)} &= MU \cdot 1 / \cos(\Phi_{1,bas}) \cdot \cos(\varphi_1) \cdot \sin(\varphi_2) \end{aligned} \quad (2)$$

$$\delta_{(100),ac} = d_{ac} \cdot \delta_{(100)}$$

$$\delta_{(110),ac} = d_{ac} \cdot \delta_{(110)}$$

$$\delta_{(110),ab} = d_{ab} \cdot \delta_{(110)}$$

$$\delta_{(100),ab} = d_{ab} \cdot \delta_{(100)} \quad (3)$$

with the normalized voltage transfer ratio defined as

$$MU := \frac{2}{\sqrt{3}} \frac{\hat{U}_2}{\hat{U}_1} \in [0, \dots, 1]. \quad (4)$$

For the sum δ_Σ of relative turn-on times of active states within one representative switching cycle ($1/2 T_p$; cf., Fig. 5), it has to be fulfilled

$$\begin{aligned} \delta_\Sigma &= \delta_{(100),ac} + \delta_{(110),ac} + \delta_{(110),ab} + \delta_{(100),ab} \\ &= \frac{MU}{\cos(\Phi_{1,bas})} \cdot \cos(\varphi_1) \cdot \cos(\varphi_2 - \pi/6) \stackrel{!}{=} [0, \dots, 1]. \end{aligned} \quad (5)$$

The global modulation index M shall be defined as the maximum of δ_Σ over the φ_1 - φ_2 plane

$$M := \max(\delta_\Sigma)_{|\varphi_1, \varphi_2} = \frac{MU}{\cos(\Phi_{1,bas})} \in [0, \dots, 1] \quad (6)$$

yielding

$$MU = M \cdot \cos(\Phi_{1,bas}). \quad (7)$$

From power considerations, one gets analogously [7]

$$MI = M \cdot \cos(\Phi_2) \quad (8)$$

for the normalized current transfer ratio, being defined as

$$MI := \frac{2}{\sqrt{3}} \frac{\hat{I}_1}{\hat{I}_2} \in [0, \dots, 1]. \quad (9)$$

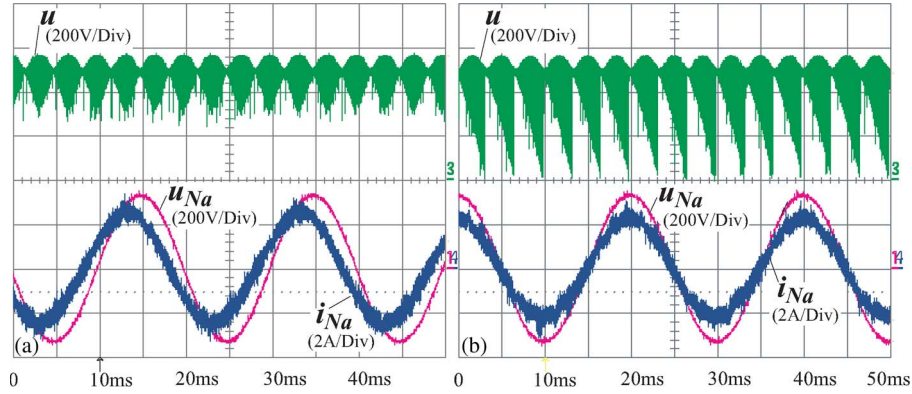


Fig. 3. Conventional indirect modulation ($Q_{1,bas}$) can be applied to adjust $\Phi_{1,bas}$ to a certain reference as long as *active* power is transferred. (a) $\Phi_{1,bas} = 0$ yields the maximum possible output voltage amplitude ($MU_{max} = 1$). (b) $\Phi_{1,bas} \approx \pi/5$ to compensate the capacitive current drawn by the input filter, thus leading to mains currents $i_{Na,b,c}$ being in phase with mains voltages $u_{Na,b,c}$. Since the local average of the dc-link voltage u is reduced in this case, the maximum output voltage amplitude is also reduced ($MU_{max} < 1$).

Therefore, the control range of basic indirect modulation is directly given by (7) and (8) or is expressed in nonnormalized form [1], [3] by

$$\hat{U}_2 = \frac{\sqrt{3}}{2} \hat{U}_1 \cdot M \cdot \cos(\Phi_{1,bas}) \quad (10)$$

$$\hat{I}_1 = \frac{\sqrt{3}}{2} \hat{I}_2 \cdot M \cdot \cos(\Phi_2). \quad (11)$$

- For *purely reactive input power*, it follows with (7), (10):

$$\begin{aligned} \Phi_{1,bas} &= \pm \pi/2 \Rightarrow P = 0 \\ &\Rightarrow \hat{U}_2 = 0 \Rightarrow Q_2 = 0. \end{aligned}$$

- For *purely reactive output power*, it follows with (8), (11):

$$\begin{aligned} \Phi_2 &= \pm \pi/2 \Rightarrow P = 0 \\ &\Rightarrow \hat{I}_1 = 0 \Rightarrow Q_1 = 0. \end{aligned}$$

Hence, it can be summarized (also, cf., [17]):

As long as one converter side (input or output) operates with pure reactive power, the other converter side does not facilitate any power—neither active power nor reactive power. Conventional indirect modulation strictly requires active power to facilitate reactive power components at the converter input and output.

This situation is graphically described in Fig. 2(a). Based on (9), which can be rewritten as

$$\hat{I}_1 = \frac{\sqrt{3}}{2} \hat{I}_2 \cdot MI \quad (9b)$$

the amplitude \hat{I}_{1q} of the reactive input current component is

$$\begin{aligned} \hat{I}_{1q} &= \hat{I}_1 \cdot \sin(\Phi_{1,bas}) \\ &= \frac{\sqrt{3}}{2} \hat{I}_2 \cdot \underbrace{\sqrt{M^2 - MU^2}}_{MI_{bas}^q} \cdot \cos(\Phi_2) \end{aligned} \quad (12)$$

whereas (7), which is equivalent to $\Phi_{1,bas} = \arccos(MU/M)$, and (8) are used to gain the final expression in (12).

In order to get the formulation of the reactive input power Q_1 , shown in Fig. 2(a), (12) just has to be scaled with a constant input voltage value

$$Q_1 = \frac{3}{2} \hat{U}_1 \cdot \hat{I}_{1q}. \quad (13)$$

According to (12) and Fig. 2(a), the reactive input current/power is not just strongly dependent on Φ_2 ; it, moreover, vanishes at full output voltage ($MU = 1$) since the modulation index is limited to $M = 1$.

Exemplary operation (measurements on VSMC prototype) of the conventional indirect modulation is shown in Fig. 3. In Fig. 3(b), a reactive input current component equivalent to $\Phi_{1,bas} \approx \pi/5$ (35°) is provided to exactly compensate the capacitive current drawn from the input filter (cf., Fig. 1) which normally (i.e., for $\Phi_{1,bas} = 0$) leads to an effective phase displacement between mains voltages and currents [cf., Fig. 3(a)]. Obviously, the formation of the dc-link voltage u is affected when operating with $\Phi_{1,bas} \neq 0$ —with increasing $|\phi_{1,bas}|$, the local average of u decreases, which finally results in $\bar{u} = 0$ and, as a consequence, in $\hat{U}_2 = 0$ for $|\Phi_{1,bas}| = \pi/2$ [cf., (7) and (10)].

Furthermore, it has to be noted that *operating an IMC/SMC with $|\Phi_{1,bas}| > \pi/6$* [like in Fig. 3(b)] requires an additional measure in the modulation algorithm. For $|\Phi_{1,bas}| > \pi/6$, the line-to-line voltages being switched into the dc-link start to get negative segments, but for IMC/SMC, we have the restriction to always provide positive dc-link voltages $u \geq 0$ since, otherwise, u will be shorted via the freewheeling diodes of the output stage. Considering the example situation in Fig. 4, one would normally choose the two discrete input stage space vectors (bc) and (ba) for the input current formation since the continuous input current reference i_1 lies in between those two. With the output voltage reference \underline{u}_2 , here given between (100) and (110), the original CMC switching cycle would be [1]

$$\begin{aligned} (110), bc \rightarrow (100), bc \rightarrow (000), bc \rightarrow \\ (000), ba \rightarrow (100), ba \rightarrow (110), ba. \end{aligned}$$

However, since (ba) in this case leads to a negative dc-link voltage $u = u_{ba} < 0$, which is equivalent to the fact

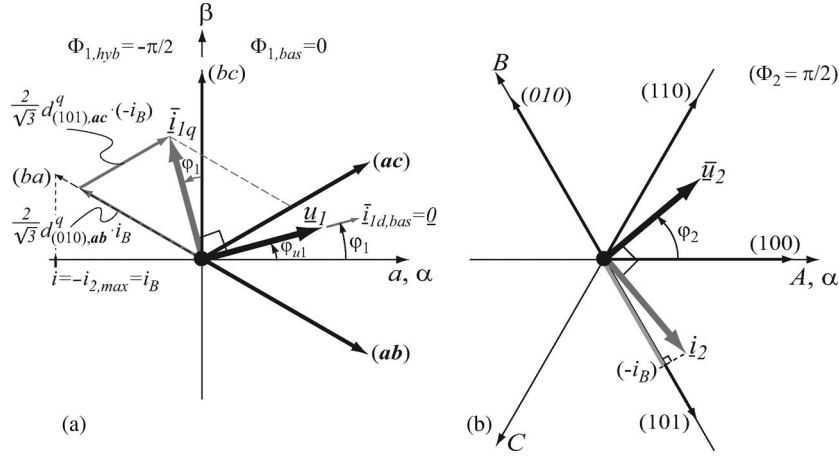


Fig. 4. Space vector diagrams of the (a) input and (b) output stage for purely reactive input and output powers. The formation of the local average value \hat{i}_{1q} of the reactive input current from discrete vectors (ba) and (ac) shown in (a) characterizes the “two-vector scheme.”

that the projection of \underline{u}_1 onto the (ba) -axis is negative, the affected switching states of both converter stages have to be *inverted*, i.e.,

$$(100), ba \Rightarrow (011), ab \text{ and } (110), ba \Rightarrow (001), ab.$$

This fulfils $u = u_{ab} \geq 0$ and keeps the original input–output behavior. Accordingly, the adapted IMC/SMC switching cycle is

$$(110), bc \rightarrow (100), bc \rightarrow (000), bc \rightarrow$$

$$(000), ab \rightarrow (001), ab \rightarrow (011), ab.$$

B. Hybrid Modulation ($\Phi_{1,bas} = 0$ and $\Phi_{1,hyb} \neq 0$)

When comparing (12) with (9b), it becomes obvious that the underbraced expression of (12) can be interpreted as a specific reactive current transfer ratio MI_{bas}^q that characterizes the basic indirect modulation ($Q_{1,bas}$).

In analogy to voltage and (active) current transfer ratio, it seems functional to define a general *reactive current* transfer ratio MI^q as

$$MI^q := \frac{2}{\sqrt{3}} \frac{\hat{I}_{1q}}{\hat{I}_2} \in [0, \dots, 1] \quad (14)$$

which will be used in the following to describe the operating limits of the hybrid modulation in normalized form.

Knowing the conventional transfer characteristic MI_{bas}^q [cf., (12) and Fig. 2(a)], it seems a desirable target to strive via hybrid modulation for a different characteristic

$$MI_{hyb}^q \neq f(\Phi_2) \quad (15)$$

being as less as possible dependent on Φ_2 .

As the numerical results in Fig. 2(b) (cf., 3-D surface) show, the proposed hybrid modulation indeed meets quite well that target specification, with just a weak dependence of MI_{hyb}^q on Φ_2 . Moreover, in contrary to conventional modulation, for large load displacement angles Φ_2 , it is even possible to facilitate a certain amount of reactive input current/power (15% at $\Phi_2 =$

$\pm\pi/2$) while at the same time supplying full output voltage [$MU = 1$; cf., dashed circle marking in Fig. 2(b)].

These two remarkable features of hybrid modulation, which relies on a decoupling of the output voltage and the input reactive current formation, allow some new practical applications of MCs, e.g., the purely reactive current of an asynchronous machine in mechanical no load operation could be used by the MC for the compensation of the reactive input filter capacitor current—even near full speed, i.e., full back EMF. Moreover, the idea to operate the MC as a FACT device [9] to compensate reactive power within the grid benefits from the possibilities hybrid modulation offers, as well as MC-based wind-energy conversion [10] does.

The control range characteristic of hybrid modulation MI_{hyb}^q , unlike (12), cannot yet be formulated by an analytically closed expression over the entire load range $0 < \Phi_2 < \pi/2$. The approach of this paper is to provide a detailed analysis of the following two extreme cases (lateral faces of Fig. 2).

- 1) $\Phi_2 = \pi/2$, i.e., $P = 0$ plane in Fig. 2(b)
 \Rightarrow the hybrid principle of *pulse merging* applies.
- 2) $\Phi_2 = 0$, i.e., $Q_2 = 0$ plane in Fig. 2(b)
 \Rightarrow the hybrid principle of *pulse compensation* applies.

The hybrid modulation schemes for both aforementioned cases ($\Phi_2 = \pi/2$ in Section III and $\Phi_2 = 0$ in Section IV) are derived, and they can be combined for application of hybrid modulation with an arbitrary load condition $0 < \Phi_2 < \pi/2$. In addition, for both aforementioned cases, the operating range limits will be given in the form of accurate analytical equations—as mentioned, the variation over Φ_2 is minor anyway.

Within Sections III-A and IV-A, the *two-vector schemes* utilizing two input stage switching states are discussed before Sections III-B and IV-B will derive the *three-vector schemes* (three input stage switching states). Finally, in Sections III-C and IV-C, the *optimum combination* of the *two- and three-vector schemes* is documented, which allows an extension of the operating limit especially at larger voltage transfer ratios $MU > 0.6$. The experimental verification of the proposed methods will be presented in Section V and will be compared to digital simulations.

The additional computational effort in comparison to conventional indirect modulation ($Q_{1,bas}$) is limited to evaluating two (or three) sine functions, two divisions, and, moreover, various distinctions of cases.

Since $\Phi_{1,bas} = 0$ applies to hybrid modulation, the parameter φ_1 in all following equations is given by the input voltage position: $\varphi_1 = \varphi_{u1}$.

III. REACTIVE INPUT CURRENT FORMATION FOR PURELY REACTIVE LOAD ($\Phi_1 = \pm\pi/2$ AND $\Phi_2 = \pi/2$)

A. Two-Vector Modulation Scheme for Purely Reactive Load

Fig. 4(a) shows the construction of the dc-link voltage for conventional modulation, which is used for each first half of a hybrid pulse period and utilizes always the two highest positive line-to-line input voltages u_{ac} and u_{ab} . Furthermore, it illustrates the separate formation of the reactive current vector \hat{i}_{1q} from the two corresponding discrete input current vectors (ba) and (ac) within the second half of each hybrid switching cycle. Thereby, both discrete current vectors are formed by that output stage phase current, which is showing the maximum instantaneous value (here, $-i_B$; cf., Fig. 4(b); maximum projection of \hat{i}_2). The effectively required input current vector (ba) would lead to negative dc-link voltage $u = u_{ba} < 0$ —for an implementation on SMC/IMC, this fact requires a *switching state inversion* of both converter stages (cf., Section II-A), i.e., by impressing the maximum negative output phase current (here, i_B) obtained by inverting the state of the output stage [to (010)], the admissible input stage state (ab) yielding $u > 0$ can be applied.¹

The resulting pulse pattern is shown in Fig. 5. The output voltage and the reactive input current formation performed in the first and second halves of the pulse period are obvious. The independent character of both formation steps expresses in the fact that, during voltage formation (first half in Fig. 5), no local average values of the input currents $i_{a,b,c}$ are generated. Analogously, when a reactive input current is formed (second half in Fig. 5), no local average of the output line–line voltages $u_{AB,BC,CA}$ is built. Since the modulation employs only two discrete input current vectors (and/or dc-link voltage levels), it is denoted as the “two-vector scheme.”

To gain the relative turn-on times for the reactive input current formation, the geometrical relations of Fig. 4(a) are formulated as

$$\frac{\sin(\frac{\pi}{3} + \varphi_1)}{\frac{2}{\sqrt{3}}(-i_{2,max}) \cdot d_{(010),ab}^q} = \frac{\cos(\varphi_1 - \frac{\pi}{6})}{\frac{2}{\sqrt{3}}i_B \cdot d_{(010),ab}^q} = \frac{\overbrace{\sin(\frac{\pi}{3})}^{\frac{\sqrt{3}}{2}}}{\hat{I}_{1q}}$$

$$\frac{\sin(\frac{\pi}{3} - \varphi_1)}{\frac{2}{\sqrt{3}}i_{2,max} \cdot d_{(101),ac}^q} = \frac{\cos(\varphi_1 + \frac{\pi}{6})}{\frac{2}{\sqrt{3}}(-i_B) \cdot d_{(101),ac}^q} = \frac{\sin(\frac{\pi}{3})}{\hat{I}_{1q}} \quad (16)$$

¹Considering a CMC, the *switching state inversion* of both virtual converter stages would effectively not change the resulting switch matrix (input to output connections), and therefore, it does not need to be performed. Nevertheless, to formally obtain consistent pulse patterns and naming conventions derived therefrom, the switching state inversion should be virtually considered also for the CMC in the following.

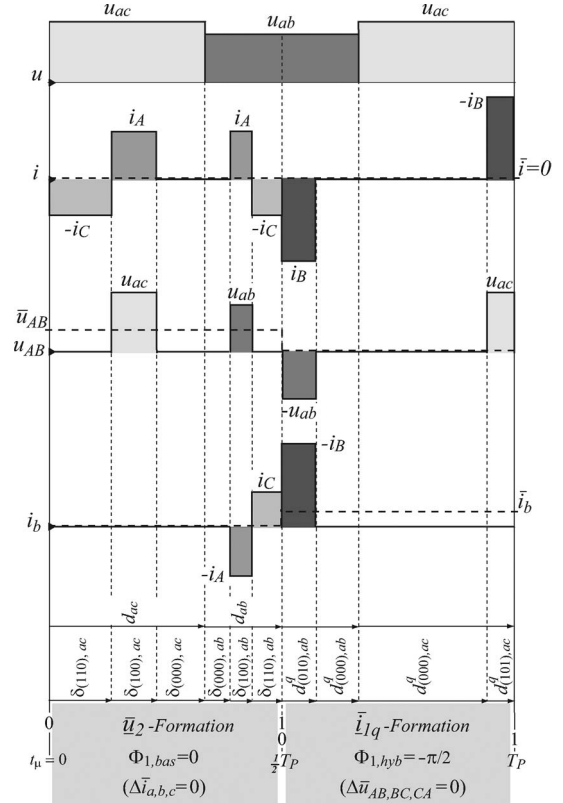


Fig. 5. Modulation scheme comprising an output voltage and a reactive input current forming pulse half period. In both intervals, only two different input current vectors [(ac) and (ab)] and/or line-to-line input voltages (dc-link voltages u_{ac} and u_{ab}) are applied. Accordingly, the modulation method is denoted as the “two-vector scheme.” Obviously, the volt seconds added to the output voltage (e.g., $\bar{u}_{AB} = 0$) during the second half of the pulse period are equal to zero, while during the first half of the pulse period, no local current average value is generated in any of the input phases (e.g., i_b).

with the maximum output phase current [cf., Fig. 4(b)] as

$$(-i_B) = -\hat{I}_2 \cdot \cos(\varphi_2 - 2\pi/3 - \pi/2) = \hat{I}_2 \cdot \cos(\varphi_2 - \pi/6). \quad (17)$$

With the definition (14), the reactive input current forming relative turn-on times follow as

$$d_{(010),ab}^q = \frac{\sqrt{3}}{2} M I^q \cdot \frac{\cos(\varphi_1 - \pi/6)}{\cos(\varphi_2 - \pi/6)}$$

$$d_{(101),ac}^q = \frac{\sqrt{3}}{2} M I^q \cdot \frac{\cos(\varphi_1 + \pi/6)}{\cos(\varphi_2 - \pi/6)}. \quad (18)$$

In order not to influence the formation of the output voltage by inserting additional current pulses, the *decouple condition*

$$0 \stackrel{!}{=} d_{(101),ac}^q \cdot u_{ac} - d_{(010),ab}^q \cdot u_{ab} \quad (19)$$

has to be fulfilled. With

$$u_{ab} = \sqrt{3}\hat{U}_1 \cdot \cos(\varphi_1 + \pi/6) \quad (20)$$

$$u_{ac} = \sqrt{3}\hat{U}_1 \cdot \cos(\varphi_1 - \pi/6) \quad (21)$$

the validity of (19) is inherently given (cf., Fig. 5; local averages of u_{AB} and i_b). Hence, the output voltage and the input current

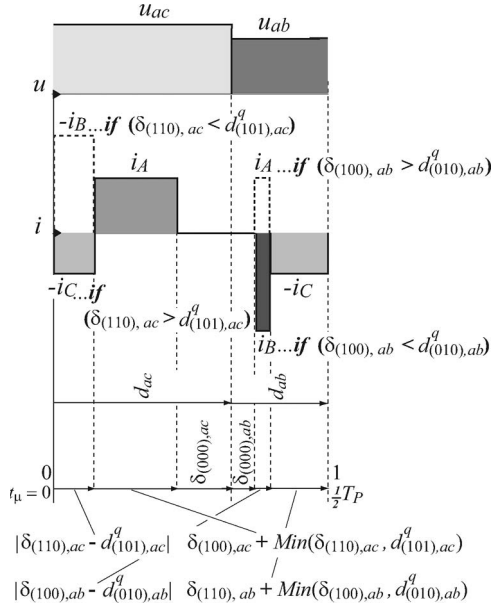


Fig. 6. Resulting final pulse pattern for the “two-vector scheme” after merging the output voltage and the input reactive current forming halves of the original pulse period (cf., Fig. 5).

formation are decoupled, which verifies the basic principle of the *hybrid modulation* method. The first half of a pulse period forms the output voltage (and *active* input current in case $\Phi_2 \neq \pi/2$) by conventional modulation, and the second pulse half period independently builds the reactive input current by utilizing the largest output phase current (and applying switching state inversions in case of SMC/IMC usage).

The voltage and current pulses resulting from the separate voltage and current formations (cf., Fig. 5) can be combined into a single pulse pattern of lower total duration, leading to an increased modulation range (input reactive current versus output voltage). This final pulse pattern is shown in Fig. 6, merging the dc-link current pulses i occurring for the same dc-link voltage level u , where the relation $i_A + i_B + i_C = 0$ of the output phase currents is considered and the sum of two pulses (two segments of the output phase currents) is expressed by the third phase current level. This principle will be denoted as *pulse merging*.

In determining the operating limit of the *two-vector scheme* as well as that of all other schemes of hybrid modulation, we again can use the left-hand side definition in (6) of the global modulation index M , being defined as the maximum of the summed relative turn-on times δ_Σ within the φ_1 - φ_2 plane. $M = 1$ represents the operating limit.

In fact, for the final pulse pattern shown in Fig. 6, we get the total relative turn-on time $\delta_{\Sigma,2V}$ of the active switching states as

$$\begin{aligned} \delta_{\Sigma,2V} = & \left| \delta_{(110),ac} - d_{(101),ac}^q \right| \\ & + \delta_{(100),ac} + \text{Min} \left(\delta_{(110),ac}, d_{(101),ac}^q \right) \\ & + \left| \delta_{(100),ab} - d_{(010),ab}^q \right| \\ & + \delta_{(110),ab} + \text{Min} \left(\delta_{(100),ab}, d_{(010),ab}^q \right). \quad (22) \end{aligned}$$

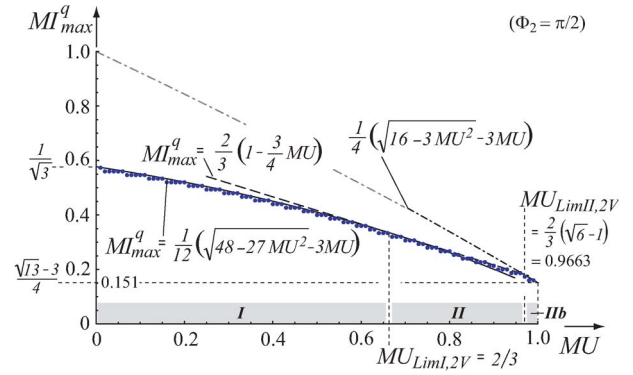


Fig. 7. Analytically derived and numerically calculated (dotted line) reactive current transfer limit of the *two-vector scheme*. $MU_{LimI,2V}$ marks the transition from the current-limiting to the voltage-limiting operating range. Remark: even at full output voltage ($MU = 1$), a reactive input current ratio of up to $MI^q = 0.151$ can still be realized.

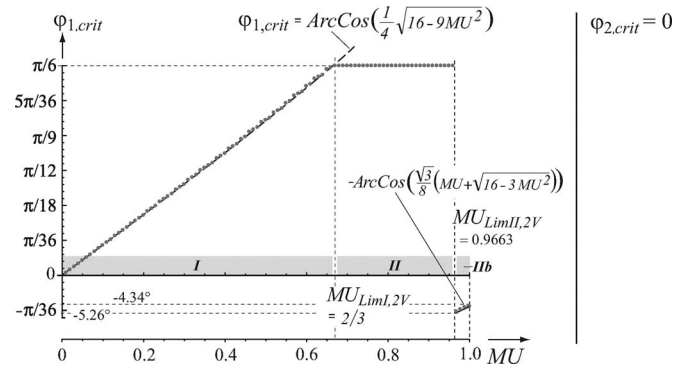


Fig. 8. Critical angle $\varphi_{1,crit,2V}$ which represents the position within a mains period where overmodulation concerning reactive input current formation occurs first. The analytical expressions (26) are clearly verified by the numerical results shown by a dotted line. $\varphi_{2,crit,2V} = 0$ is independent from MU .

The total turn-on time (22) with (2), (3), and (18) depends on four variables: φ_1 , φ_2 , MU , and MI^q . The modulation limit ($M = 1$) is reached when $\delta_{\Sigma,2V} = 1$ occurs for a certain combination of critical angles $\varphi_{1,crit}$ and $\varphi_{2,crit}$, which are associated with the maximum of $\delta_{\Sigma,2V}$ and/or with the position within a mains/load period where overmodulation appears first. Therefore, after maximum determination, we finally get a dependence of MI^q on MU , shown in Fig. 7, describing the general operating limit of the *two-vector scheme* for $\Phi_2 = \pi/2$. The limit is found by numerical calculations, but it can also be verified analytically [3], [11]. With reference to (12), it has to be pointed out that the *two-vector scheme* allows the formation of a reactive input current up to a ratio of $MI^q = 0.15$ at full output voltage ($MU = 1$).

The dependence of the critical angle $\varphi_{1,crit,2V}$ on the voltage transfer ratio MU is shown in Fig. 8. Starting from zero, $\varphi_{1,crit,2V}$ increases until $\pi/6$ is reached for $MU = 2/3$. For $2/3 < MU < 0.966$, the critical angle remains constant at $\pi/6$. The critical position in the output period is independent from MU and is fixed to $\varphi_{2,crit,2V} = 0$.

A brief explanation of the physical reasons for the operating limits that the MC shows in hybrid modulation shall be given.

The following statements are of general nature and apply to all modulation schemes proposed in this paper. The expression (22) for the total turn-on time $\delta_{\Sigma,2V}$ of a merged pulse period contains absolute and minimum functions, and therefore, it is—when intended to be solved analytically—variable in its structure. As a consequence, the solution is not a single expression but a piecewise defined set of expressions. Most proposed hybrid modulation schemes show a similar expression like (22) as their specific total turn-on time (in general, pulse merging or pulse compensation leads to this kind of expressions). They all have in common basically two physical restrictions resulting in two (or three) different intervals within the formulation of the operating limit.

1) Current-limited operating range—I

For smaller voltage transfer ratios MU (< 0.6), the reactive current forming pulses dominate the merged pulse period and/or the total turn-on time. Those pulses typically start to cause overmodulation at characteristic critical angle positions $(\varphi_{1,crit}, \varphi_{2,crit})$, which indeed get plausible when doing in-depth analysis. Accordingly, this also leads to a specific operating limit dependence $MI^q = f(MU)$. Within the following diagrams (transfer limits and critical angles), this operating range is indicated by “I”.

2) Voltage-limited operating range—II

For larger voltage transfer ratios MU (> 0.7), the output voltage forming pulses dominate the pulse period and total turn-on time. When they start causing overmodulation, this happens at different angle positions $(\varphi_{1,crit}, \varphi_{2,crit})$ as occurring for the reactive current forming pulses. As a consequence, this means a different operating limit dependence $MI^q = f(MU)$. Within the following diagrams, the voltage-limited operating range is indicated by “II”.

For the *two-vector schemes*, there exists a further voltage-limited operating interval for $MU \approx 1$, which will be marked as “IIb.”

In general, the specific conditions leading to the different operating ranges are very plausible and well understood. For the sake of brevity, they will not be explained here. Based on them, the analytical expressions describing all of the following transfer limits and critical angles were derived in a direct way. The basic approach is to always eliminate two of the four free parameters in (22) (cf., [6] and [7]).

Finally, it is worthy to mention that *optimum combination* (Section III-C) of the *two- and three-vector schemes* transfers the piecewise defined operating limit dependences into a single

dependence $MI^q = f(MU)$ being valid over the whole range of MU .

Reactive Current Transfer Limit

$$MI_{\max,2V}^q = \begin{cases} \frac{1}{12}(\sqrt{48-27MU^2}-3MU) & : 0 \leq MU \leq MU_{Lim,I} \\ \frac{2}{3}(1-\frac{3}{4}MU) & : MU_{Lim,I} \leq MU \\ & \leq MU_{Lim,II} \\ \frac{1}{4}(\sqrt{16-3MU^2}-3MU) & : MU_{Lim,II} \leq MU \leq 1 \end{cases} \quad (23)$$

with the ranges being determined by

$$MU_{Lim,I,2V} = \frac{2}{3} \approx 0.667 \quad MU_{Lim,II,2V} = \frac{2}{3}(\sqrt{6}-1) \approx 0.966. \quad (24)$$

The maximum reactive input current ratio at full voltage transfer is given as

$$MI_{\max,2V}^q(MU = 1) = \frac{\sqrt{13}-3}{4} \approx 0.151. \quad (25)$$

Critical Angle Positions

Given as (26) and (27) at the bottom of the page.

B. Three-Vector Modulation Scheme for Purely Reactive Load

The *three-vector scheme* employs input current space vectors for the current formation, which are directly neighboring the desired reactive input current vector \hat{i}_{1q} (formed in the average over a pulse period), e.g., (bc) and (ba) , as shown in Fig. 9(a). Accordingly, in contrast to the *two-vector scheme*, for the *three-vector scheme*, the sign of φ_1 has to be considered. Based on the geometrical relations of Fig. 9, we have, for the additional turn-on times for $\varphi_1 \geq 0$

$$d_{(010),ab}^q = \frac{\sqrt{3}}{2} MI^q \cdot \frac{\sin(\varphi_1)}{\cos(\varphi_2 - \pi/6)} \\ d_{(101),bc}^q = \frac{\sqrt{3}}{2} MI^q \cdot \frac{\cos(\varphi_1 + \pi/6)}{\cos(\varphi_2 - \pi/6)} \quad (28)$$

where the negative current pulse i_B has to be assigned to (ab) .

$$\varphi_{1,crit,2V} = \begin{cases} \arccos\left(\frac{1}{4}\sqrt{16-9MU^2}\right) & : 0 \leq MU \leq MU_{Lim,I} \\ \pi/6 & : MU_{Lim,I} \leq MU \leq MU_{Lim,II} \\ -\arccos\left(\frac{\sqrt{3}}{8}(MU + \sqrt{16-3MU^2})\right) & : MU_{Lim,II} \leq MU \leq 1 \end{cases} \quad (26)$$

$$\varphi_{2,crit,2V} = 0 \quad (27)$$

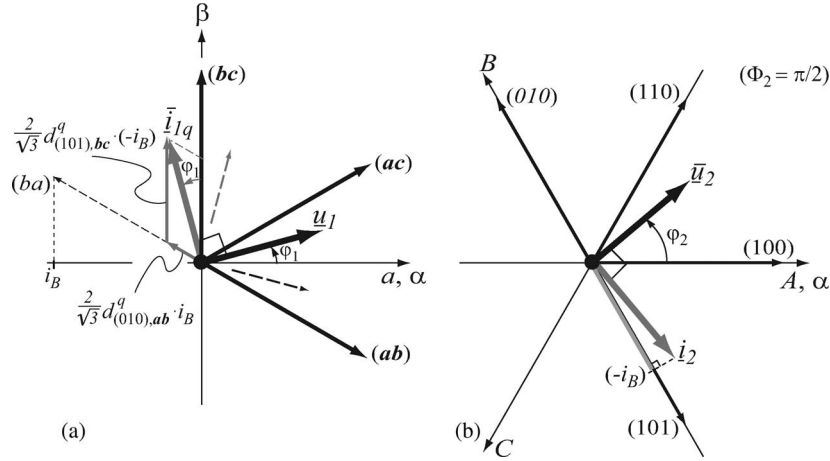


Fig. 9. Space vector diagrams of the (a) input and (b) output stage for purely reactive input and output powers. The formation of the reactive input current vector \bar{i}_{1q} (local average value) using the vectors (ba) and (bc) , as shown in (a), characterizes the “three-vector scheme” (for the output voltage formation, (ac) and (ab) are employed, so, in total, three different vectors are utilized within each pulse period).

In analogy for $\varphi_1 < 0$

$$\begin{aligned} d_{(101),ac}^q &= \frac{\sqrt{3}}{2} MI^q \cdot \frac{\sin(|\varphi_1|)}{\cos(\varphi_2 - \pi/6)} \\ d_{(010),cb}^q &= \frac{\sqrt{3}}{2} MI^q \cdot \frac{\cos(|\varphi_1| + \pi/6)}{\cos(\varphi_2 - \pi/6)} \end{aligned} \quad (29)$$

is valid where the negative current pulse i_B has to be assigned to (cb) . The corresponding *decouple condition* for the *three-vector scheme*

$$0 \stackrel{!}{=} d_{(101),bc}^q \cdot u_{bc} - d_{(010),ab}^q \cdot u_{ab} \quad (30)$$

(exemplary for $\varphi_1 \geq 0$) is fulfilled with (20) and

$$u_{bc} = \sqrt{3} \hat{U}_1 \cdot \sin(\varphi_1) \quad (31)$$

which basically verifies the functionality also of this hybrid scheme.

As shown in Figs. 10 and 11 for the “three-vector scheme”, a merging of current and voltage pulses is possible only for that input stage switching state appearing in both pulse half intervals (in the case at hand (ab)). Since one reactive current forming pulse ($-i_B$) has to stay fully unmerged in the final pulse pattern (Fig. 11), this, in the end, leads to the fact that, at full output voltage ($MU = 1$), *no* reactive input current can be formed ($MI^q = 0$) by the *three-vector scheme*. On the other hand, the total turn-on time of the two reactive current forming pulses is minimized due to the more advantageous alignment of the two employed discrete current space vectors that are both located directly next to the desired reference vector \bar{i}_{1q} . Latter argument translates into an increased reactive current transfer ratio (up to $MI^q = 1$) for small output voltages (cf., Fig. 12) when compared to the *two-vector scheme*.

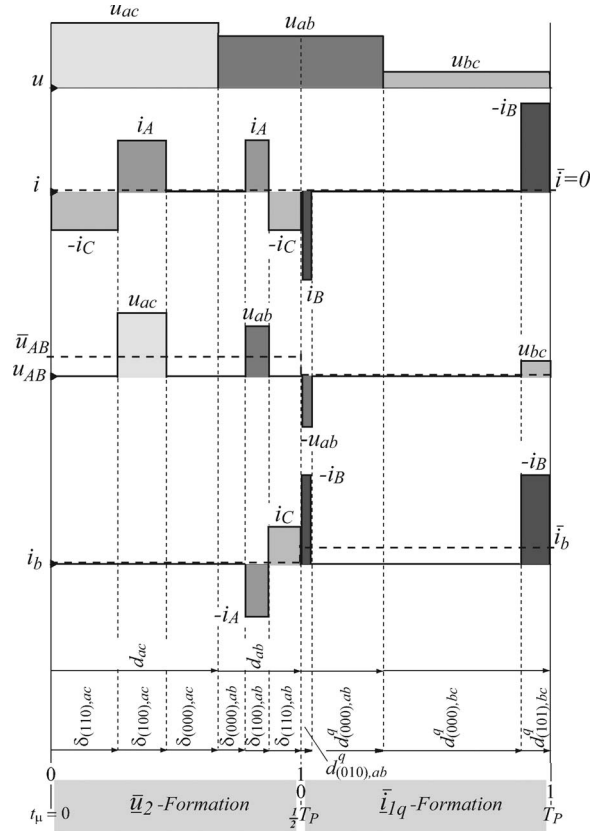


Fig. 10. Modulation based on the “three-vector scheme” for $\varphi_1 \geq 0$. In total, three different dc-link voltage levels (ac), (ab) , and (bc) and/or input current vectors are employed within each pulse period for the output voltage and the input current formation. The local average values of the output voltage (e.g., \bar{u}_{AB}) and the input reactive current (e.g., \bar{i}_b) are decoupled from each other.

The total turn-on time of the active switching states then results as

$$\begin{aligned} \delta_{\Sigma,3V} &= \delta_{(110),ab} + \text{Min} \left(\delta_{(100),ab}, d_{(010),ab}^q \right) \\ &+ \left| \delta_{(100),ab} - d_{(010),ab}^q \right| + \delta_{(100),ac} + \delta_{(110),ac} + d_{(101),bc}^q. \end{aligned} \quad (32)$$

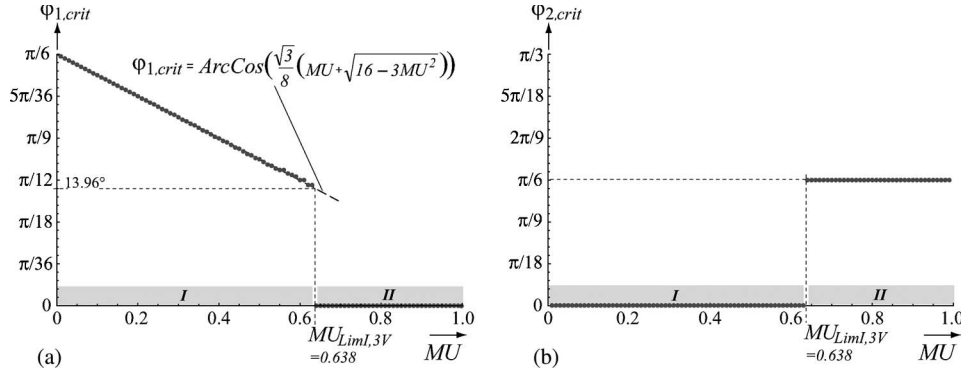


Fig. 13. Dependence of the critical angle values (a) $\varphi_{1,crit,3V}$ and (b) $\varphi_{2,crit,3V}$ of the *three-vector scheme* on MU . Changing from the current-limited operating range ($MU = 0, \dots, 0.638$) to the voltage-limited range ($MU = 0.638, \dots, 1$) clearly affects both angle values representing a maximum of $\delta_{\Sigma,3V}$ in the φ_1 - φ_2 plane. The analytical expression (35) for $\varphi_{1,crit,3V}$ coincides with the numerical results (dotted line).

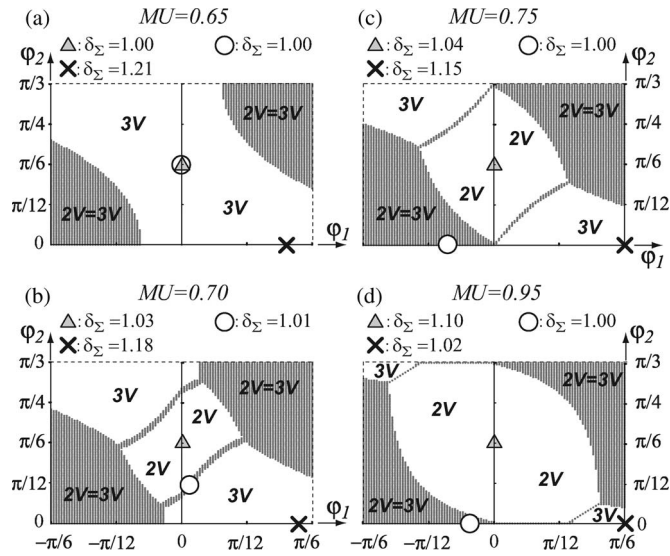


Fig. 14. Domains within the φ_1 - φ_2 plane defining the optimum application areas of the *two- or three-vector modulation scheme* with respect to minimum δ_{Σ} for different values of MU . The dark color marks areas where $\delta_{\Sigma,2V} = \delta_{\Sigma,3V}$ is valid. Remark: the maxima of δ_{Σ} for the *two-vector, three-vector, and optimum schemes* are occurring symmetrically to the plane center point. For the sake of clarity, the maxima are only marked in the positive φ_1 half plane. Legend: \times is the maximum of $\delta_{\Sigma,2V}$, \blacktriangle is the maximum of $\delta_{\Sigma,3V}$, and \circ is the maximum of $\delta_{\Sigma,opt}$.

times, the operating limit will be extended by using this scheme. This can be clearly seen in Fig. 15. As shown in Fig. 14(b)–(d), in the vicinity of the maximum of the *three-vector scheme*, the *two-vector scheme* showing a lower $\delta_{\Sigma,2V}$ is applied and vice versa.

When approaching full output voltage [Fig. 14(d)], the domain of the *three-vector scheme* vanishes, and for $MU \approx 1$, the *two-vector scheme* constitutes the *optimum modulation scheme*.

As shown in Fig. 16, the numerical analysis confirms that the operating limit of the *optimum combination modulation* coincides within the entire output voltage range $MU = [0, \dots, 1]$, with the favorable limit defined by (33a) for the *three-vector scheme* in the current-limited operating range only (cf., Fig. 12). Below (38) expresses this fact.

Reactive Current Transfer Limit

$$MI_{max,opt}^q = \frac{1}{4}(\sqrt{16 - 3MU^2} - 3MU) : 0 \leq MU \leq 1. \quad (38)$$

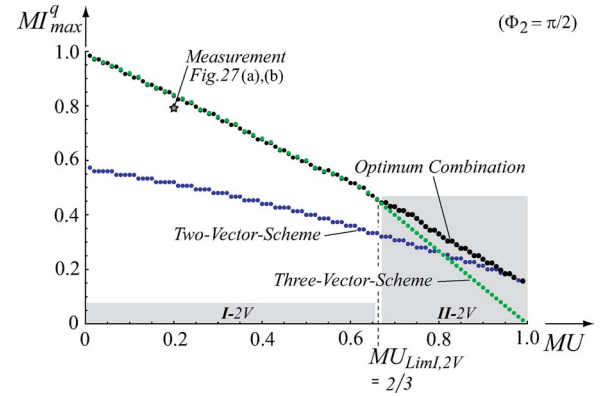


Fig. 15. Comparison of the operating limits of the modulation schemes. Up to $MU_{Lim,2V}$, the *three-vector scheme* results in the maximum value of MI^q . From there, MI^q can be increased by changing to the *two-vector scheme* within sections of the φ_1 - φ_2 plane, as shown in Fig. 14. For full output voltage ($MU = 1$), the MI^q limit is defined by the *two-vector scheme*.

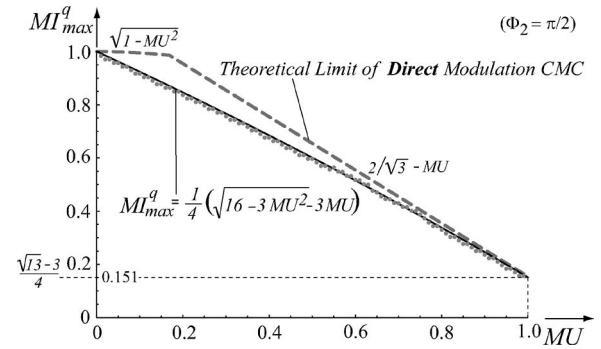


Fig. 16. Numerical analysis proves the maximum reactive current transfer limit achieved by *optimum modulation* to stay for the entire output voltage range $MU = [0, \dots, 1]$ on the limit (33a) valid for the *three-vector scheme* in the current-limited operating range. Furthermore, shown is the theoretical limit of the reactive current transfer for the CMC according to [4].

Moreover, (38) is identical to (23c), describing the limit of the *two-vector scheme* in the voltage-limited operating range (IIb) and, hence, verifying formally that both modulation schemes provide exactly the same reactive input current $MI^q = 0.151$ at $MU = 1$.

In Fig. 16, additionally marked (bold dashed line) is the theoretical reference limit of the reactive current transfer as presented in [4], which can be achieved with the more complex

direct modulation applied on the CMC. Particularly, in the upper output voltage region ($MU > 0.5$), both modulation methods show very similar limits.

Finally, it should be pointed out that the implementation of the proposed *optimum combination* modulation scheme could be achieved with just marginally increasing the realization effort since all turn-on times (i.e., only (3) and (28) since (18) can be derived from (28) by summation) have to be calculated within the modulation algorithm. Therefore, just the sums (22) and (32) have to be compared, and the modulation scheme showing the lower total turn-on time has to be selected [cf., (37)].

IV. REACTIVE INPUT CURRENT COMPONENT FORMATION FOR PURELY ACTIVE LOAD ($\Phi_2 = 0$)

A. Two-Vector Modulation Scheme for Purely Active Load

For the following considerations, the load is assumed to draw a purely *active* current, i.e., $\Phi_2 = 0$. Considering this zero displacement angle at the output stage, the space vector diagram Fig. 4 is still valid.

Contrary to $\Phi_2 = \pi/2$, now the current in the output phase ($-C$) shows the largest positive instantaneous value. Accordingly, in the formulas for the additional turn-on times, only the phase shift of φ_2 in the cosine terms of the denominator has to be adapted

$$\begin{aligned} d_{(001),ab}^q &= \frac{\sqrt{3}}{2} M I^q \cdot \frac{\cos(\varphi_1 - \pi/6)}{\cos(\varphi_2 - \pi/3)} \\ d_{(110),ac}^q &= \frac{\sqrt{3}}{2} M I^q \cdot \frac{\cos(\varphi_1 + \pi/6)}{\cos(\varphi_2 - \pi/3)}. \end{aligned} \quad (39)$$

Fig. 17 shows a pulse period of the hybrid modulation scheme for an active load comprising an output voltage/active input current forming half period and a subsequent half period dedicated to the formation of a reactive input current component. This scheme is largely equivalent to the *two-vector scheme* employed for purely reactive load (cf., Fig. 5). As the main difference here, in total, only two different output phase currents are switched into the dc-link. Therefore, the merging of current pulses results in (partial) *pulse compensation*.

For example, in Fig. 17, the pulse i_C occurring for $u = u_{ab}$ in the second pulse half period overcompensates the neighboring pulse ($-i_C$) of the first half period and reduces the total turn-on time. The second pulse of the reactive current forming interval ($-i_C$) occurring for $u = u_{ac}$ cannot be compensated, but it has to be added to the pulse ($-i_C$) of the voltage forming interval, thereby increasing the total turn-on time. This, in the end, results in the final pulse pattern shown in Fig. 18.

Considering Fig. 18, we have, for the total turn-on time of the active switching states

$$\begin{aligned} \delta_{\Sigma,2V,act} &= \delta_{(110),ac} + d_{(110),ac}^q + \delta_{(100),ac} \\ &+ \delta_{(100),ab} + \left| \delta_{(110),ab} - d_{(001),ab}^q \right|. \end{aligned} \quad (40)$$

For geometrical reasons, (40) is asymmetric in $\varphi_1 = [-\pi/6, \dots, \pi/6]$ and shows a clear minimum in the negative

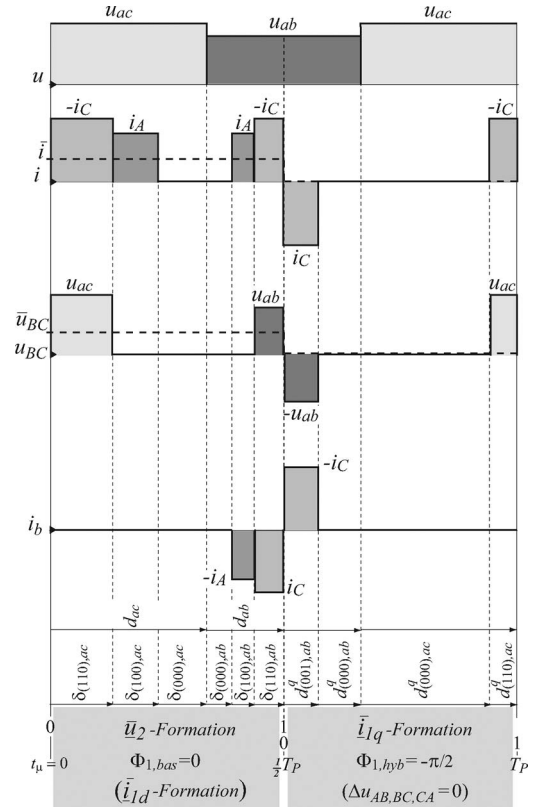


Fig. 17. Hybrid modulation for reactive input current formation in case of purely active load. The first half of each pulse period is dedicated to the formation of the output voltage and the active input current component. Subsequently, the reactive input current component is formed in the second pulse half period. In both half intervals, only two different input current vectors [(ac) and (ab) in the case at hand] are applied, and/or two line-to-line input voltages are switched into the dc-link ($u = u_{ac}, u_{ab}$). Accordingly, the modulation scheme is denoted as “two-vector scheme for purely active load.” No volt seconds are added to the output voltage (e.g., u_{BC}) within the second half of the pulse period.

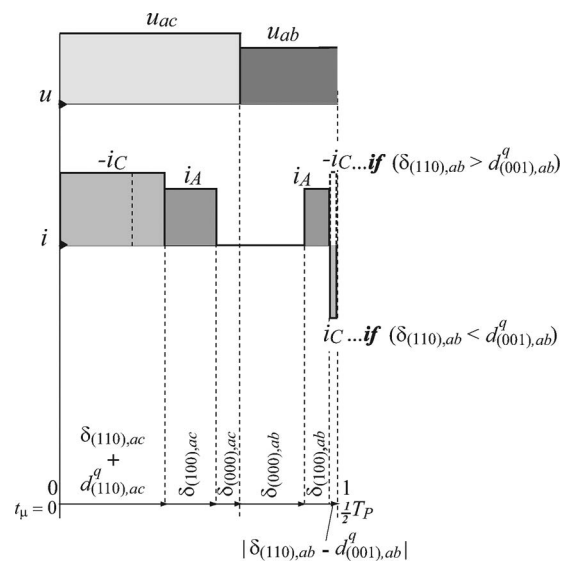


Fig. 18. Resulting final pulse pattern for the “two-vector scheme for purely active load” after merging the output voltage and the input reactive current forming halves of the pulse period shown in Fig. 17.

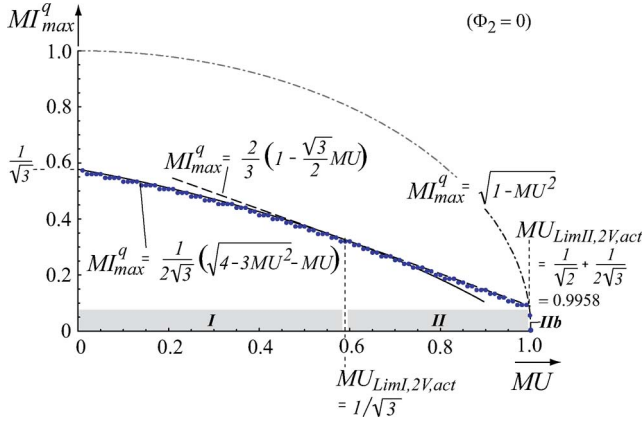


Fig. 19. Analytically derived and numerically calculated (dotted line) transfer limits of the *two-vector scheme* for purely active load. There is a clear transition within the voltage-limited operating range at $MU = 0.996$.

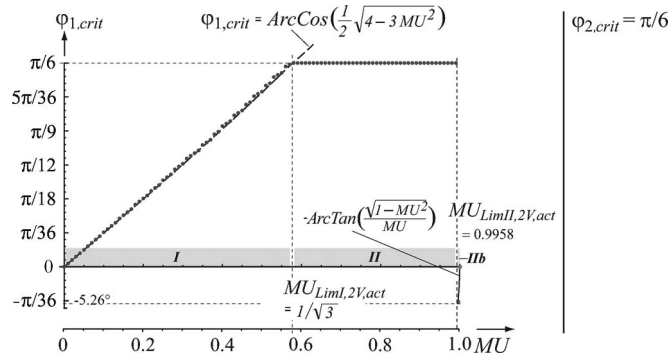


Fig. 20. Critical mains phase angle $\varphi_{1,crit,2V,act}$. After the transition to the voltage-limiting range ($MU > 1/\sqrt{3}$), the critical mains angle stays constant at $\varphi_{1,crit,2V,act} = \pi/6$ until $MU = 0.996$ is reached. Thereafter, at full output voltage, finally, negative angle values $[-5.26^\circ, \dots, 0]$ limit the modulation.

φ_1 half plane. The numerical and analytical analysis of (40) yields the operating limit of the *two-vector scheme* for purely active load shown in Fig. 19 and the critical positions $\varphi_{1,crit,2V}$ within a mains period shown in Fig. 20. The critical angle in the output period is independent from MU and is fixed to $\varphi_{2,crit,2V} = \pi/6$

Reactive Current Transfer Limit

$$MI_{max,2V,act}^q = \begin{cases} \frac{1}{2\sqrt{3}}(\sqrt{4-3MU^2} - MU) & : 0 \leq MU \leq MU_{Lim,I} \\ \frac{2}{3}\left(1 - \frac{\sqrt{3}}{2}MU\right) & : MU_{Lim,I} < MU \leq MU_{Lim,II} \\ \sqrt{1-MU^2} & : MU_{Lim,II} < MU \leq 1 \end{cases} \quad (41)$$

with the ranges defined by

$$MU_{Lim,I,2V,act} = \frac{1}{\sqrt{3}} \approx 0.577$$

$$MU_{Lim,II,2V,act} = \frac{1 + \sqrt{6}}{2\sqrt{3}} \approx 0.996. \quad (42)$$

It should be pointed out that the transfer limit (41c) valid in the voltage-limited operating range *III*b (i.e., $MU > 0.996$)

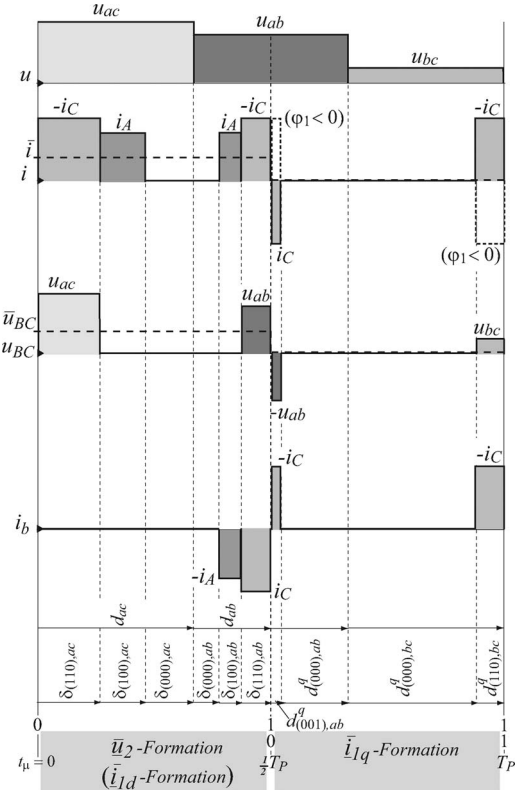


Fig. 21. Hybrid modulation denoted as “*three-vector scheme* for purely active load.” In total, three different input current vectors and/or dc-link voltage levels (*ac*), (*ab*), and (*bc*) are employed within each pulse period. *Remark*: the pulse pattern shown is valid for $\varphi_1 > 0$. In order to point out the main difference in case of $\varphi_1 < 0$, the dc-link current pulses are also shown with inverse polarity. Moreover, in this case, the dc-link voltage labels u_{ac} and u_{ab} have to be exchanged, and u_{bc} has to be replaced by u_{cb} (cf., Fig. 22).

is identical with that limit of conventional indirect modulation ($Q_{1,bas}$) for $\Phi_2 = 0$ (cf., Figs. 19 and 25).

Critical Angle Positions

$$\varphi_{1,crit,2V,act}$$

$$= \begin{cases} \arccos\left(\frac{1}{2}\sqrt{4-3MU^2}\right) & : 0 \leq MU \leq MU_{Lim,I} \\ \pi/6 & : MU_{Lim,I} < MU \leq MU_{Lim,II} \\ -\arctan\left(\frac{\sqrt{1-MU^2}}{MU}\right) & : MU_{Lim,II} < MU \leq 1 \end{cases} \quad (43)$$

$$\varphi_{2,crit,2V,act} = \pi/6. \quad (44)$$

B. Three-Vector Modulation Scheme for Purely Active Load

Considering $\Phi_2 = 0$, again, the space vector diagram in Fig. 9 is basically valid and yields the additional turn-on times: for $\varphi_1 \geq 0$

$$d_{(001),ab}^q = \frac{\sqrt{3}}{2} MI^q \cdot \frac{\sin(\varphi_1)}{\cos(\varphi_2 - \pi/3)}$$

$$d_{(110),bc}^q = \frac{\sqrt{3}}{2} MI^q \cdot \frac{\cos(\varphi_1 + \pi/6)}{\cos(\varphi_2 - \pi/3)} \quad (45)$$

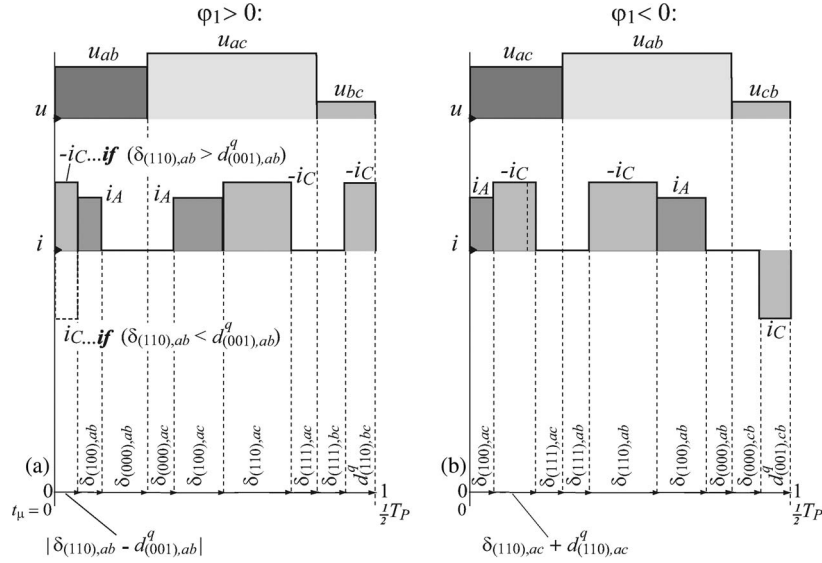


Fig. 22. Resulting final pulse pattern for the “three-vector scheme for purely active load.” For $\varphi_1 > 0$, (a) input current and/or output voltage pulses occurring for $u = u_{ab}$ in the first and second halves of the pulse period shown in Fig. 21 with inverse polarity are compensating each other. In contrast, for $\varphi_1 < 0$, (b) pulses occurring for the common dc-link voltage level $u = u_{ac}$ show the same polarity. In consequence, no reduction of the total turn-on time can be achieved. *Remark:* the sequence of dc-link voltage levels has changed compared to Fig. 21. This is done for the same reasons as mentioned in Fig. 11.

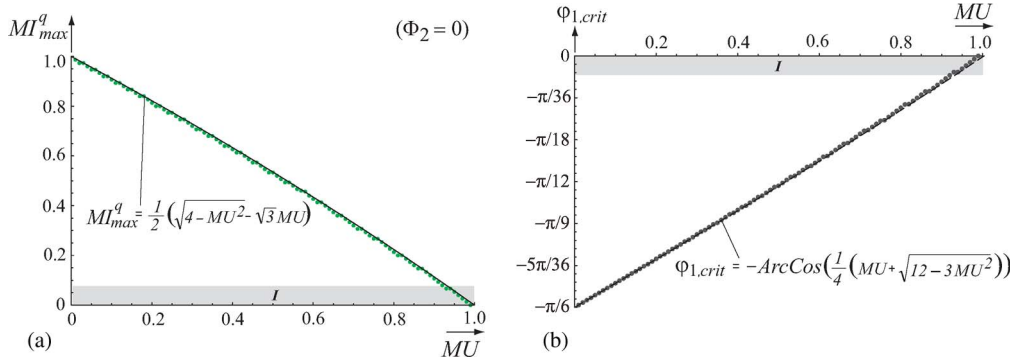


Fig. 23. *Three-vector scheme* for $\Phi_2 = 0$. (a) Reactive current transfer limit and (b) critical position $\varphi_{1,crit,3V,act}$ within a mains period. As the modulation scheme does not facilitate a reduction of the total turn-on time for $\varphi_1 < 0$, the maximum of $\delta_{\Sigma,3V,act}$ associated with $\varphi_{1,crit,3V,act}$ is located in the negative φ_1 half plane. The critical load angle remains constant at $\varphi_{2,crit,3V,act} = \pi/6$.

for $\varphi_1 < 0$ instead

$$\begin{aligned} d_{(110),ac}^q &= \frac{\sqrt{3}}{2} MI^q \cdot \frac{\sin(|\varphi_1|)}{\cos(\varphi_2 - \pi/3)} \\ d_{(001),cb}^q &= \frac{\sqrt{3}}{2} MI^q \cdot \frac{\cos(|\varphi_1| + \pi/6)}{\cos(\varphi_2 - \pi/3)}. \end{aligned} \quad (46)$$

Fig. 21 shows a hybrid pulse period of the *three-vector scheme for purely active load*. Considering the (partial) *pulse compensation*, Fig. 21 is finally transferred to the pulse pattern shown in Fig. 22. It has to be pointed out that the pulse compensation is not possible at all for $\varphi_1 < 0$. Therefore, in this case, no reduction of the total turn-on time results [cf., (47)]. Accordingly, only the worst-case situation $\varphi_1 < 0$ has to be analyzed further (numerically and analytically) in order to determine the associated operating limit.

From Fig. 22(b) it follows for $\varphi_1 < 0$ and/or for the larger total turn-on time:

$$\begin{aligned} \delta_{\Sigma,3V,act} &= \delta_{(110),ac} + d_{(110),ac}^q + \delta_{(100),ac} \\ &\quad + \delta_{(100),ab} + \delta_{(110),ab} + d_{(001),cb}^q. \end{aligned} \quad (47)$$

Since no turn-on time reduction is possible for $\varphi_1 < 0$, a pronounced maximum of $\delta_{\Sigma,3V,act}$ is located in the negative φ_1 half plane. This asymmetry is also documented by the dependence of $\varphi_{1,crit,3V}$, shown in Fig. 23(b).

The current transfer limit in Fig. 23(a) is determined by the pulse pattern in Fig. 22(b), allowing no pulse compensation for $\varphi_1 < 0$.

Accordingly, (47) contains just continuous terms, finally resulting in operating limit characteristics, as shown in Fig. 23, not showing any discontinuous transitions over the entire output voltage range $MU = [0, \dots, 1]$ [cf., (48)–(50)].

Reactive Current Transfer Limit

$$\begin{aligned} MI_{\max,3V,act}^q &= \frac{1}{2} (\sqrt{4 - MU^2} - \sqrt{3} \cdot MU) \\ &: 0 \leq MU \leq 1. \end{aligned} \quad (48)$$

Critical Angle Positions

$$\begin{aligned} \varphi_{1,crit,3V,act} &= -\arccos\left(\frac{1}{4}(MU + \sqrt{12 - 3MU^2})\right) \\ &: 0 \leq MU \leq 1 \end{aligned} \quad (49)$$

$$\varphi_{2,crit,3V,act} = \pi/6. \quad (50)$$

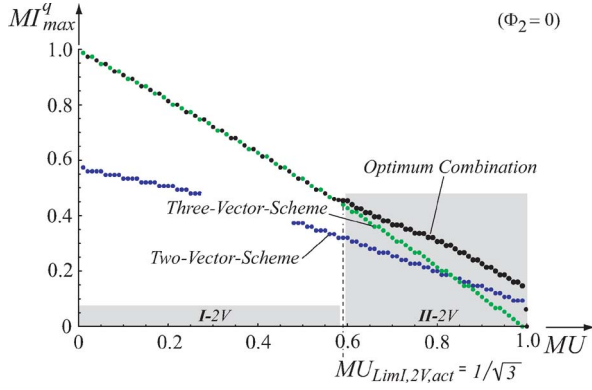


Fig. 24. Comparison of the operating limits of the modulation schemes. The *optimum combination* modulation is identical to the *three-vector scheme* up to $MU_{Lim,I,2V,act}$. From there, the reactive input current formation capability is increased by locally employing the *two-vector scheme*.

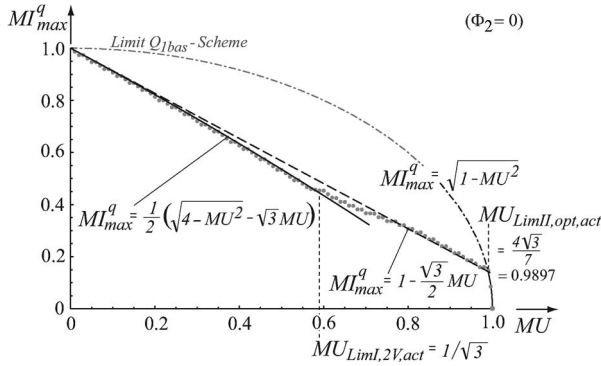


Fig. 25. Operating limit of *optimum combination* modulation for $\Phi_2 = 0$. For full output voltage ($MU > 0.99$), the *optimum* hybrid modulation is limited to the reactive input current formation capability of the conventional $Q_{1,bas}$ modulation scheme (i.e., $MI^q = 0$ for $MU = 1$). Obviously, when operating with purely active load ($\Phi_2 = 0$), the conventional $Q_{1,bas}$ scheme (dashed gray curve) seems superior to the hybrid modulation.

C. Optimum Combination of the Two- and Three-Vector Schemes for Purely Active Load

Due to the asymmetry of both schemes, i.e., the low values of $\delta_{\Sigma,2V,act}$ occurring for the *two-vector scheme* for $\varphi_1 < 0$ and the low values of $\delta_{\Sigma,3V,act}$ given for the *three-vector scheme* for $\varphi_1 > 0$, the *optimum combination* allows a larger extension of the operating range as compared to operation with purely reactive load (cf., Section III-C). This is clearly documented by Fig. 24 (cf., [6, Fig. 20]). Analytically derived operating limits (51) are visualized in Fig. 25 and are compared to the numerical results also shown in Fig. 24.

Reactive Current Transfer Limit

$$MI_{max,opt,act}^q = \begin{cases} \frac{1}{2} (\sqrt{4 - MU^2} - \sqrt{3} MU) & : 0 \leq MU \leq MU_{Lim,I} \\ 1 - \frac{\sqrt{3}}{2} MU & : MU_{Lim,I} < MU \\ & \leq MU_{Lim,II} \\ \sqrt{1 - MU^2} & : MU_{Lim,II} < MU \leq 1 \end{cases} \quad (51)$$

with (cf., Fig. 25)

$$MU_{Lim,I,2V,act} = \frac{1}{\sqrt{3}} \approx 0.577$$

$$MU_{Lim,II,opt,act} = \frac{4\sqrt{3}}{7} \approx 0.990. \quad (52)$$

V. SIMULATION AND EXPERIMENTAL VERIFICATION

The proposed *hybrid* modulation schemes and the calculated operating limits have been verified by digital simulation [Fig. 26(a) and (c)] and by experimental results (Figs. 26(b) and (d) and 27). Therein, Fig. 26 shows the *two-vector scheme* at $\Phi_2 = \pi/2$. Measurements from the *three-vector scheme* at $\Phi_2 = \pi/2$ are shown in Fig. 27 for an operating point being marked within the identified operating limit of Fig. 15. All experimental results are taken from a 6.5-kW VSMC.

The simulation of the *two-vector scheme* (at $\Phi_2 = \pi/2$) with the same operating parameters as that for the VSMC prototype when taking the measurements shows exactly [shown in Fig. 26(c)] the expected amplitude \hat{I}_{1q} of the input current i_a . Generally, in both measurements, the capacitive current of the input filter capacitor has to be taken into account. This current component (which cannot be avoided in a real system) increases the measured amplitude in Fig. 26(d) by $\Delta \hat{I}_{1q} \approx 350$ mA compared to the simulation. Accordingly, that portion can also be roughly seen when the MC does not operate at all or when it operates with purely reactive output power and with $\Phi_1 = 0$.

Exactly, this situation is shown in Fig. 27(c) and (d) for reference. When considering this capacitor-caused bias current component, we do also see, for the *three-vector scheme* (at $\Phi_2 = \pi/2$) in Fig. 27(a) and (b), the expected reactive input current amplitude \hat{I}_{1q} theoretically resulting from the marked operating point in Fig. 15 (which is close to the operating limit). Fig. 27(e) and (f) shows the basic option in compensating the capacitive filter current by an intentionally modulated inductive input current ($\Phi_{1,hyb} = \pi/2$). As can be clearly noticed in Fig. 27(a) and (e), the *three-vector scheme* is characterized by the dc-link voltage (envelope) being switched between all three positive line–line input voltage levels.

In general, the simulation and experimental analysis verify very well the hybrid modulation schemes.

VI. CONCLUSION

In this paper, a new—indirect modulation based—approach to significantly extend the reactive input power operating range of an MC has been proposed. This modulation principle, denoted as *hybrid modulation*, enables a set of new modulation schemes (*two-vector*, *three-vector*, and *optimum schemes*) being applicable to purely reactive load ($\Phi_2 = \pi/2$; *pulse merging* applies) and to purely active load ($\Phi_2 = 0$; *pulse compensation* applies). Therefore, in total, six new single schemes were described and analyzed in detail, where all of them are implementable with very low additional calculation effort (two sine functions, two divisions, and several distinctions of cases). With the *pulse merging* principle (presented for $\Phi_2 = \pi/2$)

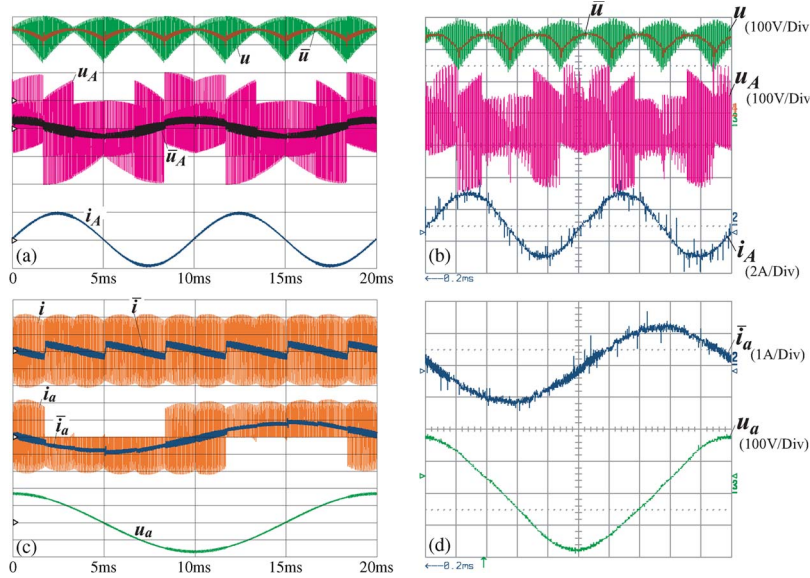


Fig. 26. (a) and (c) Digital simulation and (b) and (d) measurements of the VSMC modulated by the *two-vector scheme* with purely reactive current at the output and input stage ($\Phi_1 = -\pi/2$ and $\Phi_2 = \pi/2$). $MU = 0.2$, and $MI^q = 0.44$. Further parameters: $\hat{U}_1 = 170$ V, $L_{Load} = 25$ mH, $f_1 = 50$ Hz, and $f_2 = 100$ Hz.

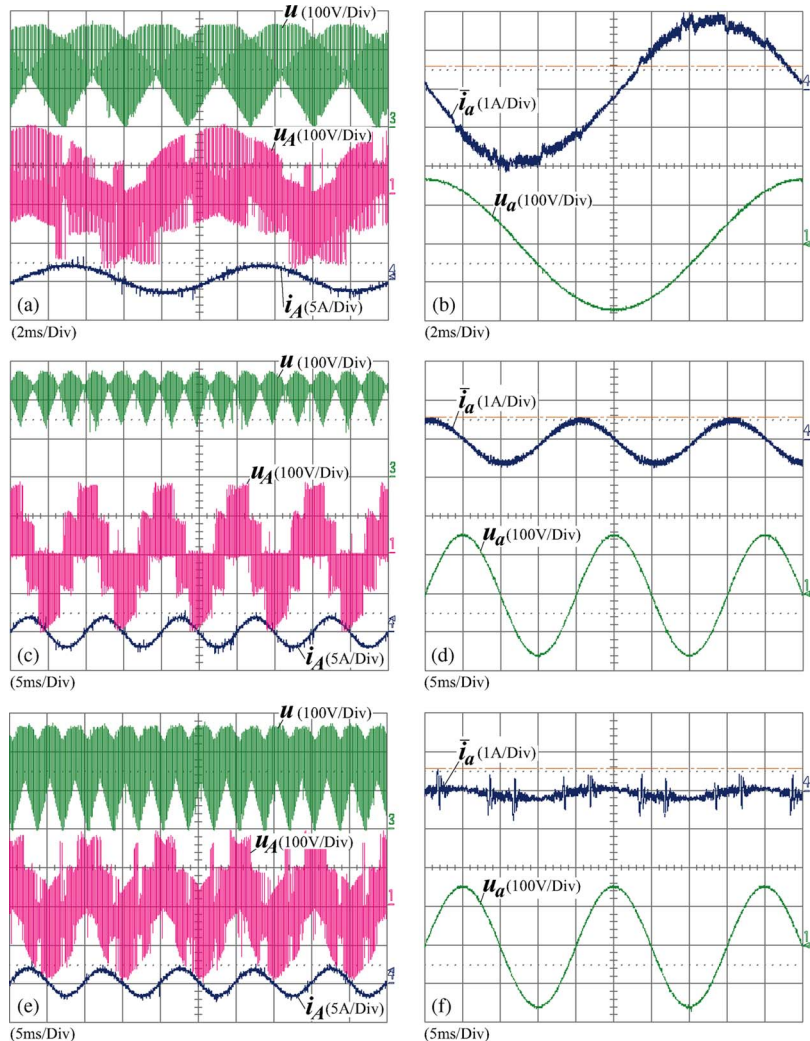


Fig. 27. Experimental verification of the *three-vector scheme* with VSMC ($\Phi_2 = \pi/2$ and $MU = 0.2$). (a) and (b) Conditions like the ones marked in Fig. 15 ($MI^q = 0.79$). (c) and (d) For reference: conventional modulation with $MI^q = 0$ (over 50 ms). (e) and (f) $MI^q = 0.4$ and $\Phi_{1,hyb} = +\pi/2$ approximately compensates the capacitive current drawn by the input filter (over 50 ms). Further parameters: the same as those in Fig. 26.

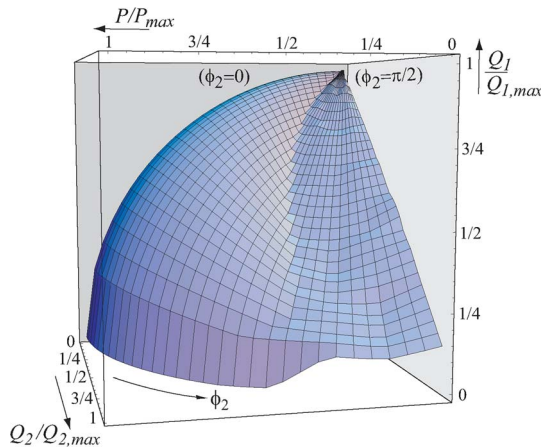


Fig. 28. Maximized control range of an indirectly modulated MC achieved by optimum mixed mode modulation, i.e., basic scheme ($Q_{1,bas}$) or hybrid scheme ($Q_{1,hyb}$) (cf., Fig. 2(a) to notice improvement in comparison to conventional modulation). For $\Phi_2 > \pi/3$, the proposed hybrid modulation is superior.

and the *pulse compensation* (shown for $\Phi_2 = 0$), the hybrid modulation can be generalized to an arbitrary load condition $0 < |\Phi_2| < \pi/2$.

As the results show, the *optimum combination* modulation gives the best transfer performance for very low additional effort. From Section IV, it can be concluded that the *hybrid modulation* for a purely active load ($\Phi_2 = 0$) is in an inferior position compared to conventional indirect modulation ($Q_{1,bas}$). However, for increasing load displacements Φ_2 and smaller output voltages or generally for $\Phi_2 > \pi/3$, *hybrid modulation* becomes superior to conventional indirect modulation (cf., Fig. 28). The largest reactive power control range (over $0 < |\Phi_2| < \pi/2$ by indirect modulation) seems achievable by an optimum *mixed mode* modulation, i.e., either conventional modulation ($\Phi_{1,bas} \neq 0, \Phi_{1,hyb} = 0$) or hybrid modulation ($\Phi_{1,bas} = 0, \Phi_{1,hyb} \neq 0$).

Considering the resulting extended MC control range in Fig. 28, the usage of *hybrid (indirect) modulation* seems attractive for a couple of new MC applications ([9]–[11]), e.g., in the field of wind-energy conversion, and is also, in this respect, highly competitive to the more complex direct modulation approach [12]–[15].

REFERENCES

- [1] J. W. Kolar, M. Baumann, F. Schafmeister, and H. Ertl, "Novel three-phase ac–dc–ac sparse matrix converter, Part I and II," in *Proc. 17th Annu. IEEE Appl. Power Electron. Conf.*, Dallas, TX, Mar. 10–14, 2002, vol. 2, pp. 777–791.
- [2] L. Wei and T. A. Lipo, "A novel matrix converter topology with simple commutation," in *Conf. Rec. IEEE IAS Annu. Meeting*, Chicago, IL, Sep. 30–Oct. 4, 2001, vol. 3, pp. 1749–1754.
- [3] L. Huber and D. Borojovic, "Space vector modulated three-phase to three-phase matrix converter with input power factor correction," *IEEE Trans. Ind. Appl.*, vol. 31, no. 6, pp. 1234–1246, Nov./Dec. 1995.
- [4] J. Igney and M. Braun, "A new matrix converter modulation strategy maximizing the control range," in *Proc. 35th Annu. IEEE Power Electron. Spec. Conf.*, Aachen, Germany, Jun. 21–24, 2004, pp. 2875–2880.
- [5] F. Schafmeister and J. W. Kolar, "Novel modulation schemes for conventional and sparse matrix converters facilitating reactive power transfer independent of active power flow," in *Proc. 35th Annu. IEEE Power Electron. Spec. Conf.*, Aachen, Germany, Jun. 21–24, 2004, pp. 2917–2923.

- [6] F. Schafmeister and J. W. Kolar, "Novel hybrid modulation schemes extending the reactive power control range of conventional and sparse matrix converters operating at maximum output voltage," in *Proc. 11th Int. Power Electron. Motion Control Conf.*, Riga, Latvia, Sep. 2–4, 2004, [CD-ROM].
- [7] F. Schafmeister, "Indirekte & Sparse Matrix Konverter," Ph.D. dissertation no. 17428, ETH Zurich, Zurich, Switzerland, 2007.
- [8] F. Schafmeister and J. W. Kolar, "Verfahren zur Kopplung der ein- und ausgangsseitigen Blindleistungsflüsse dreiphasiger Matrixkonverter," May 29, 2009, Swiss Patent CH698150, filed Jun. 21, 2004, granted.
- [9] N. Holtmark and M. Molinas, "Reactive power compensation using an indirectly space vector-modulated matrix converter," in *Proc. IEEE Int. Symp. Ind. Electron.*, Bari, Italy, Jul. 4–7, 2010, pp. 2455–2460.
- [10] R. Cárdenas, R. Pena, P. Wheeler, J. Clare, and G. Asher, "Control of the reactive power supplied by a WESC based on induction generator fed by a matrix converter," *IEEE Trans. Ind. Electron.*, vol. 56, no. 2, pp. 429–438, Feb. 2009.
- [11] H. Nguyen, H. Lee, and T. Chun, "Input power factor compensation algorithms using a new direct-SVM method for matrix converter," *IEEE Trans. Ind. Electron.*, vol. 58, no. 1, pp. 232–243, Jan. 2011.
- [12] J. Igney and M. Braun, "Space vector modulation strategy for conventional and indirect matrix converters," in *Proc. 11th Eur. Conf. Power Electron. Appl.*, Dresden, Germany, Sep. 11–14, 2005, pp. P.1–P.10.
- [13] D. Casadei, G. Serra, A. Tani, and L. Zarri, "Matrix converter modulation strategies: A new general approach based on space-vector representation of the switch state," *IEEE Trans. Ind. Electron.*, vol. 49, no. 2, pp. 370–381, Apr. 2002.
- [14] J. Igney, "Steuerverfahren für matrixumrichter unter der besonderen Betrachtung der Eingangsblindleistung," Ph.D. dissertation, Univ. Karlsruhe, Karlsruhe, Germany, 2006.
- [15] H. Hojabri, H. Mokhtari, and L. Chang, "A generalized technique of modeling, analysis, and control of a matrix converter using SVD," *IEEE Trans. Ind. Electron.*, vol. 58, no. 3, pp. 949–959, Mar. 2011.
- [16] J. W. Kolar and F. Schafmeister, "Novel modulation schemes minimizing the switching losses of sparse matrix converters," in *Proc. 29th Annu. Conf. IEEE Ind. Electron. Soc.*, Roanoke, VA, Nov. 2–6, 2003, pp. 2085–2090.
- [17] J. W. Kolar, F. Schafmeister, S. D. Round, and H. Ertl, "Novel three-phase ac–ac sparse matrix converters," *IEEE Trans. Power Electron.*, vol. 22, no. 5, pp. 1649–1661, Sep. 2007.



Frank Schafmeister (S'03–M'07) was born in Germany in 1974. He received the Dipl.-Ing. degree in electrical engineering from the University of Paderborn, Germany, in 2001 and the Ph.D. degree from the Swiss Federal Institute of Technology (ETH) Zurich, Switzerland, in 2007.

In 2001, he was a Research Associate with the Power Electronic Systems Laboratory, ETH Zurich, where he was working in the field of three-phase power conversion. His special focus was on design, modulation, and control of ac–ac matrix converters of different topologies. In 2007, he joined DELTA Energy Systems, Soest, Germany, as a Research Engineer, working on the implementation of new technologies into customized high power supplies. His current research interests include digital control of various power topologies, resonant topologies, and power conversion efficiency improvement for single-phase, three-phase, and inverter applications.

Dr. Schafmeister is member of the German Association for Electrical, Electronic and Information Technologies VDE.



Johann W. Kolar (F'10) received the M.Sc. and Ph.D. degrees (*summa cum laude/promotio sub auspiciis praesidentis rei publicae*) from the University of Technology Vienna, Vienna, Austria.

Since 1984, he has been working as an Independent International Consultant in close collaboration with the University of Technology Vienna in the fields of power electronics, industrial electronics, and high-performance drives. He was appointed as a Professor and the Head of the Power Electronic Systems Laboratory, Swiss Federal Institute of Technology (ETH) Zurich, Zurich, Switzerland, on February 1, 2001, which was awarded as the leading academic research institution in power electronics in Europe by the European Power Supplies Manufacturers Association in 2006. He also received an Erskine Fellowship from the University of Canterbury, Christchurch, New Zealand, in 2003. He initiated and/or he is the founder/cofounder of four spin-off companies targeting ultrahigh-speed drives, multidomain/level simulation, ultracompact/efficient converter systems, and pulsed power/electronic energy processing. He has proposed numerous novel PWM converter topologies and modulation and control concepts, e.g., the Vienna rectifier, the Swiss rectifier, and the three-phase ac-ac sparse matrix converter. He has published over 350 scientific papers in international journals and conference proceedings and has filed more than 75 patents. The focus of his current research is on ac-ac and ac-dc converter topologies with low effects on the mains, e.g., for power supply of data centers, more-electric aircraft, and distributed renewable energy systems. Further main areas of research are the realization of ultracompact and ultraefficient converter modules employing the latest power semiconductor technology (SiC and GaN), novel concepts for cooling and EMI filtering, multidomain/scale modeling/simulation and multiobjective optimization, physical-model-based lifetime prediction, pulsed power, and ultrahigh-speed and bearingless motors.

Dr. Kolar is a member of the Institute of Electrical Engineers of Japan (IEEJ). He received the Best Transactions Paper Award from the IEEE Industrial Electronics Society in 2005, the Best Paper Award from the International Conference on Power Electronics (ICPE) in 2007, the First Prize Paper Award from the IEEE IAS IPCC in 2008, the IEEE IECON Best Paper Award from the IES PETC in 2009, the 2009 IEEE Power Electronics Society Transaction Prize Paper Award, and the 2010 Best Paper Award of the IEEE/ASME TRANSACTIONS ON MECHATRONICS. He is a member of international steering committees and technical program committees of numerous international conferences in the field (e.g., the Director of the Power Quality Branch of the International Conference on Power Conversion and Intelligent Motion). He is the founding Chairman of the IEEE PELS Austria and Switzerland Chapter and the Chairman of the Education Chapter of the EPE Association. From 1997 to 2000, he was an Associate Editor of the IEEE TRANSACTIONS ON INDUSTRIAL ELECTRONICS, and since 2001, he has been an Associate Editor of the IEEE TRANSACTIONS ON POWER ELECTRONICS. Since 2002, he has also been an Associate Editor of the *Journal of Power Electronics* of the Korean Institute of Power Electronics and a member of the Editorial Advisory Board of the *IEEJ Transactions on Electrical and Electronic Engineering*.